Dalton Transactions

ROYAL SOCIETY OF CHEMISTRY

PAPER

View Article Online
View Journal | View Issue

Open Access Article. Published on 05 January 2023. Downloaded on 11/6/2025 11:33:04 PM.
This article is licensed under a Creative Commons Attribution 3.0 Unported Licence.

Check for updates

Cite this: *Dalton Trans.*, 2023, **52**, 3596

An investigation of steric influence on the reactivity of $Fe^{V}(O)(OH)$ tautomers in stereospecific C–H hydroxylation†

Mainak Mitra,[a,b] Alexander Brinkmeier,[a] Yong Li,[a] Margarida Borrell,[c] Arnau Call,[c] Julio Lloret Fillol,[d] Michael G. Richmond,[e] Miquel Costas *[c] and Ebbe Nordlander *[a]

Two new tetradentate N4 ligands ($\mathbf{L^{N4}}$), $\mathbf{L^{N4}}$ = $^{\mathbf{Me2,Me2}}$**PyzTACN** (1-(2-(3,5-dimethyl-1*H*-pyrazol-1-yl) ethyl)-4,7-dimethyl-1,4,7-triazacyclononane) and $^{\mathbf{Me2,Me}}$**ImTACN** (1-((1-methyl-1*H*-imidazol-1-yl) methyl)-4,7-dimethyl-1,4,7-triazacyclononane) have been synthesized and their corresponding Fe(II) complexes [Fe^{II}($^{\mathbf{Me2,Me2}}$**PyzTACN**)(CF_3SO_3)$_2$], $\mathbf{1^{Pz}}$, and [Fe^{II}($^{\mathbf{Me2,Me}}$**ImTACN**)(CF_3SO_3)$_2$], $\mathbf{1^{Im}}$, have been prepared and characterized. Complexes $\mathbf{1^{Pz}}$ and $\mathbf{1^{Im}}$ catalyse the hydroxylation of C–H bonds of alkanes with excellent efficiencies, using hydrogen peroxide as oxidant. The high H/D kinetic isotope effect values for C–H hydroxylation, large normalized tertiary/secondary C–H (C3/C2) bond selectivities in adamantane oxidation, and high degrees of stereoretention in the oxidation of *cis*-1,2-dimethylcyclohexane are indicative of metal-based oxidation processes. The complexes also catalyse the oxidation of cyclooctene to form its corresponding epoxide and *syn*-diol. For $\mathbf{1^{Pz}}$ the epoxide is the main product, while for the analogous complex $\mathbf{1^{Im}}$ the *syn*-diol predominates. The active oxidant is proposed to be an [($\mathbf{L^{N4}}$)Fe^{V}(O)(OH)]$^{2+}$ species ($\mathbf{2^{Pz}}$, $\mathbf{L^{N4}}$ = $^{\mathbf{Me2,Me2}}$**PyzTACN** and $\mathbf{2^{Im}}$, $\mathbf{L^{N4}}$ = $^{\mathbf{Me2,Me}}$**ImTACN**) which may exist in two tautomeric forms related by a proton shift between the oxo and hydroxo ligands. Isotope labelling experiments show that the oxygen atom in the hydroxylated products originates from both water and hydrogen peroxide, and labelling experiments involving oxygen atom transfer to sterically bulky substrates provide indirect information on the steric influence exerted by the two ligands in the relative reactivities of the two hypervalent iron tautomers. Based on these labelling studies, the steric influence exerted by each of the ligands towards the relative reactivity of the oxo ligands of the corresponding pair of Fe(V)(O)(OH) tautomers can be derived. Furthermore, this steric influence can be gauged relative to related complexes/ligands.

Received 7th March 2022,
Accepted 28th November 2022

DOI: 10.1039/d2dt00725h

rsc.li/dalton

Introduction

Over the last two decades, a number of transition metal-based complexes have been developed as catalysts for selective oxidations of hydrocarbons.[1,2] Iron is often a metal of choice for such catalytic transformations because it is inexpensive, non-toxic and highly abundant.[3,4] In nature, oxygenases carry out a wide range of organic substrate oxidations, and many of them contain iron in their active sites.[5–8] These iron oxygenases are usually highly selective towards specific C–H bonds and utilize atmospheric oxygen as the ultimate oxidant.[6] An example is the Rieske oxygenase family of non-heme iron enzymes, which contains an Fe(II) center bound to two histidine residues and one aspartate in the active site.[8] This family of bacterial enzymes catalyzes the *cis*-dihydroxylation of arenes *via* activation of dioxygen (Scheme 1) as the first step in the biodegradation of pollutants.[6] Although the identity of the active species remains a matter of debate, one of the mechanistic proposals favours a formally high valent Fe(V) center bound to an oxo and a hydroxo groups that are *cis* to each other (Scheme 1).[5,6,9] These species hydroxylate aliphatic C–H bonds and *syn*-dihydroxylate alkenes and arenes. The mechanism of C–H hydroxylation is proposed to consist of a two-step process that is directly related to the

[a]*Chemical Physics, Department of Chemistry, Lund University, Box 124, SE-221 00 Lund, Sweden. E-mail: Ebbe.Nordlander@chemphys.lu.se*
[b]*Department of Chemistry, Burdwan Raj College, Aftab Avenue, W.B. 713104, India*
[c]*QBIS-CAT, Department of Chemistry and Institut de Quimica Computacional i Catàlisi, University of Girona, Campus Montilivi, E-17071 Girona, Spain. E-mail: miquel.costas@udg.edu*
[d]*Institute of Chemical Research of Catalonia (ICIQ), The Barcelona Institute of Science and Technology, Avinguda Paisos Catalans 16, 43007 Tarragona, Spain*
[e]*Department of Chemistry, University of North Texas, Denton, Texas 76203, USA*

† Electronic supplementary information (ESI) available: ESI-MS, ^{1}H-NMR, UV/Vis and FT-IR spectra of complexes $\mathbf{1^{Pz}}$ and $\mathbf{1^{Im}}$. CCDC 2154313 ($\mathbf{1^{Pz}}$). For ESI and crystallographic data in CIF or other electronic format see DOI: **https://doi.org/10.1039/d2dt00725h**

This journal is © The Royal Society of Chemistry 2023

Open Access Article. Published on 05 January 2023. Downloaded on 11/6/2025 11:33:04 PM.
This article is licensed under a Creative Commons Attribution 3.0 Unported Licence.

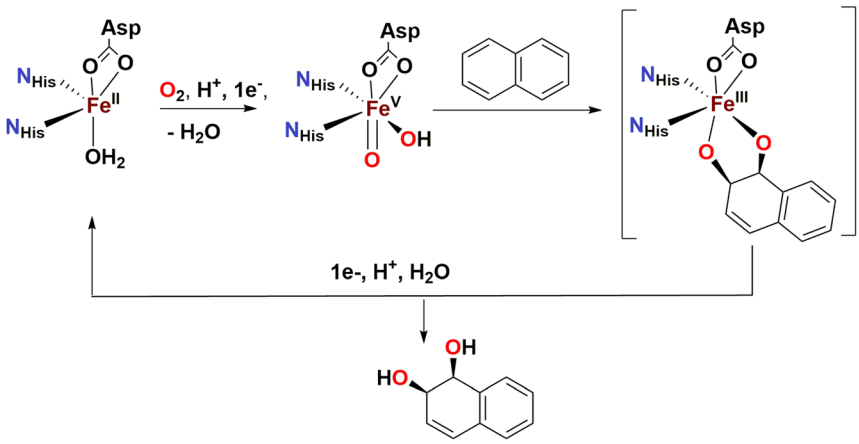

Scheme 1 Proposed reaction mechanism for *cis*-dihydroxylation by naphthalene dioxygenase.

canonical "oxygen rebound" mechanism of the cytochrome P450 family of heme oxygenases; this mechanism involves (i) abstraction of a hydrogen atom from a substrate C–H bond by the oxo group to form a transient substrate-based alkyl radical and an Fe(IV)$(OH)_2$ moiety, and (ii) interaction of the alkyl radical with one of the hydroxyl groups of the Fe(IV)$(OH)_2$ moiety to form the product.[10] The reaction with alkenes is envisioned to occur *via* a 3 + 2 reaction of the Fe(V)(O)(OH) moiety with the olefin site, akin to *syn*-dihydroxylations performed by OsO_4, RuO_4 or MnO_4^-. With the reactivities of non-heme iron oxygenases such as Rieske oxygenases serving as an inspiration, several mononuclear non-heme iron catalysts have been developed to address the challenging oxidations of poorly reactive C–H and C=C bonds.[11–15]

The Fe(**PyTACN**) family of complexes (**PyTACN** = 1-(2-pyridylmethyl)-4,7-dimethyl-1,4,7-triazacyclononane) has been shown to mediate stereospecific C–H hydroxylation with excellent efficiencies.[16–18] Isotope labelling and theoretical studies strongly indicate that the oxidations occur *via* the involvement of high valent Fe(V) oxo intermediates.[16–18] The reactive intermediate in C–H hydroxylation reactions has been identified as a highly electrophilic $[Fe^{V}(O)(OH)(\mathbf{L^{N4}})]^{2+}$ oxidant ($\mathbf{L^{N4}}$ corresponds to tetradentate TACN-based ligands), which is formed *via* water-assisted O–O cleavage of the hydroperoxo precursor $[Fe^{III}(OOH)(OH_2)(\mathbf{L^{N4}})]^{2+}$.[19] The $[Fe^{V}(O)(OH)(\mathbf{L^{N4}})]^{2+}$ oxidant can exist in two tautomeric forms, corresponding to structures $\mathbf{O_A}$ and $\mathbf{O_B}$ in Scheme 2, because of the unsymmetric nature of the tetradentate TACN-derivatives that serve as ligands.[18] The two tautomers differ in the relative positions of the *cis*-coordinated oxo and hydroxo groups, and are connected through a prototopic oxo-hydroxo tautomerism. Investigations have been made on the influence on C–H hydroxylation reactions exerted by manipulating the electronic and steric properties *via* introduction of different groups (*e.g.* Me, F, NO_2, NMe_2) in α and γ positions of the pyridine ring of the **PyTACN** ligand.[18,20] These studies indicated that electronic properties of the groups in γ position on the pyridine ring have minor influence on the relative reactivities between the two tautomers $\mathbf{O_A}$ and $\mathbf{O_B}$ while, instead, the steric properties of the groups in the α position of the pyridine ring do.[18,20] The discrimination between the relative reactivities of $\mathbf{O_A}$ and $\mathbf{O_B}$ was found to be more pronounced in cases of substrates containing tertiary C–H bonds.[18] Replacement of the pyridyl arm of the **PyTACN** ligand with a corresponding (*N*-methyl)benzimidazolyl arm led to the formation of the complex $[Fe^{II}(^{Me2,Me}\mathbf{BzImTACN})(CF_3SO_3)_2]$, $\mathbf{1^{BzIm}}$.[21] Reactivity (catalytic oxidation) studies on this complex were entirely in keeping with the proposed formation of an active Fe(V)(O)(OH) oxidant, and it was found that the (*N*-methyl)benzimidazolyl moiety exerts an effect in the relative reactivities of $\mathbf{O_A}$ and $\mathbf{O_B}$ that lies in between that of pyridyl and α-Me-pyridyl moieties. This effect parallels the steric demand of the heterocyclic ligand, as deduced from an inspection of the crystal structures of the corresponding ferrous complexes. Importantly, $\mathbf{1^{BzIm}}$ was

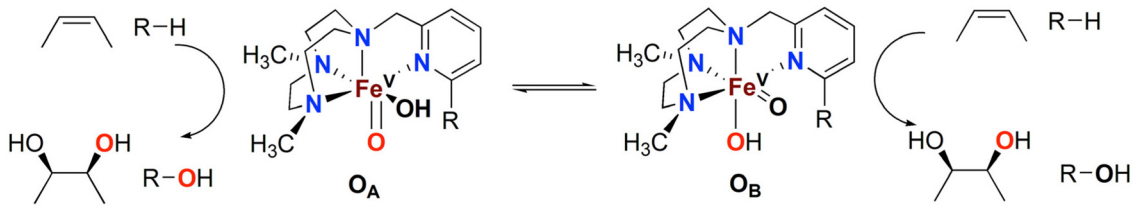

Scheme 2 Oxidation of alkanes (R–H) and olefins by the two tautomers, $\mathbf{O_A}$ and $\mathbf{O_B}$, observed in reactions catalysed by the Fe(**PyTACN**) family of complexes.[18,20,21]

Open Access Article. Published on 05 January 2023. Downloaded on 11/6/2025 11:33:04 PM.
This article is licensed under a Creative Commons Attribution 3.0 Unported Licence.

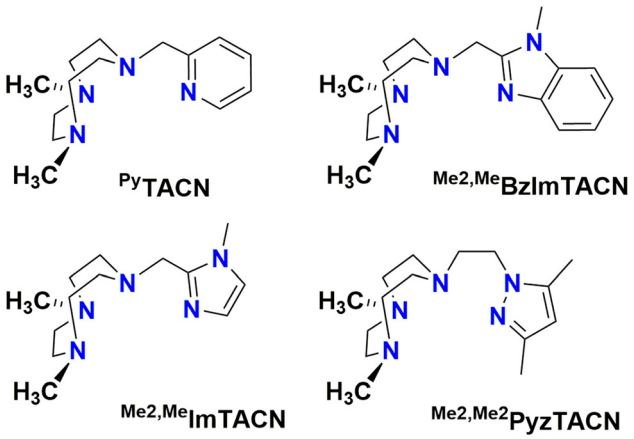

Fig. 1 Structures of the tetradentate ligands **PyTACN**, ^{Me2,Me}**BzImTACN**, ^{Me2,Me}**ImTACN** and ^{Me2,Me2}**PyzTACN** discussed in this work.

found to maintain high efficiencies and selectivities in the hydroxylation of alkanes and olefins.[21]

In this work, we describe $[Fe^{II}(\mathbf{L^{N4}})(CF_3SO_3)_2]$ complexes bearing two new tetradentate N4 ligands, ^{Me2,Me2}**PyzTACN** and ^{Me2,Me}**ImTACN** (Fig. 1). These ligands are based on the **PyTACN** ligand scaffold, where the pyridyl side arm is replaced by (*N*-methyl)imidazolyl and 3,5-dimethylpyrazolyl arms, respectively. The ligand ^{Me2,Me2}**PyzTACN** contains an ethylene spacer connecting one of the amines of the triazacyclononane (TACN) ring and the N(2) atom of the 3,5-dimethylpyrazole, whereas the corresponding spacer is a methylene in ^{Me2,Me}**ImTACN**, in direct correspondence to the ligand frameworks of **BzImTACN** and **PyTACN**. The (*N*-methyl)imidazolyl moiety (pK_a of conjugate acid: 7.06) is more basic than (*N*-methyl)benzimidazolyl (pK_a of conjugate acid: 5.41) and pyridine (pK_a of conjugate acid: 5.22), while 3,5-dimethylpyrazole is less basic (pK_a of conjugate acid: 4.12). Collectively, the different ligands discussed above are thus expected to span a range of steric and electronic demands, while yielding structurally similar Fe(II) complexes that in turn may give rise to analogous Fe(V)(O)(OH) complexes that will exist in tautomeric forms (*cf.* Scheme 2). Thus, the ligands are expected to exert not only electronic but also steric influence on the relative reactivities of the Fe(V)(O)(OH) $\mathbf{O_A}$ and $\mathbf{O_B}$ tautomers operating in the C–H hydroxylation reactions. An investigation of the catalytic hydroxylation and olefin oxidation reactions effected by these two iron complexes is described herein. Isotope labelling studies and computational methods have also been performed to elucidate the reaction mechanism(s) and to assess the steric and electronic influence of the ligands on the reactivities of the iron catalysts.

Results and discussion

Syntheses and characterization

The two new tetradentate N4 ligands ^{Me2,Me2}**PyzTACN** and ^{Me2,Me}**ImTACN** were synthesized by reaction of TACN·3HBr with the corresponding chloromethylene/chloroethylene precursor complex of the five membered heterocyclic ring (pyrazole and imidazole) as described in Scheme 3 (*cf.* Experimental section and ESI† for detailed characterization).

The corresponding Fe(II) complexes were synthesized inside a dry atmosphere box. Reaction of one equiv. of $[Fe^{II}(CH_3CN)_2(CF_3SO_3)_2]$ with one equiv. of ^{Me2,Me2}**PyzTACN** in dry THF resulted in precipitation of the corresponding complex $[Fe^{II}(^{Me2,Me2}\mathbf{PyzTACN})(CF_3SO_3)_2]$ ($\mathbf{1^{Pz}}$), which was collected by filtration, washed with a small amount of THF and

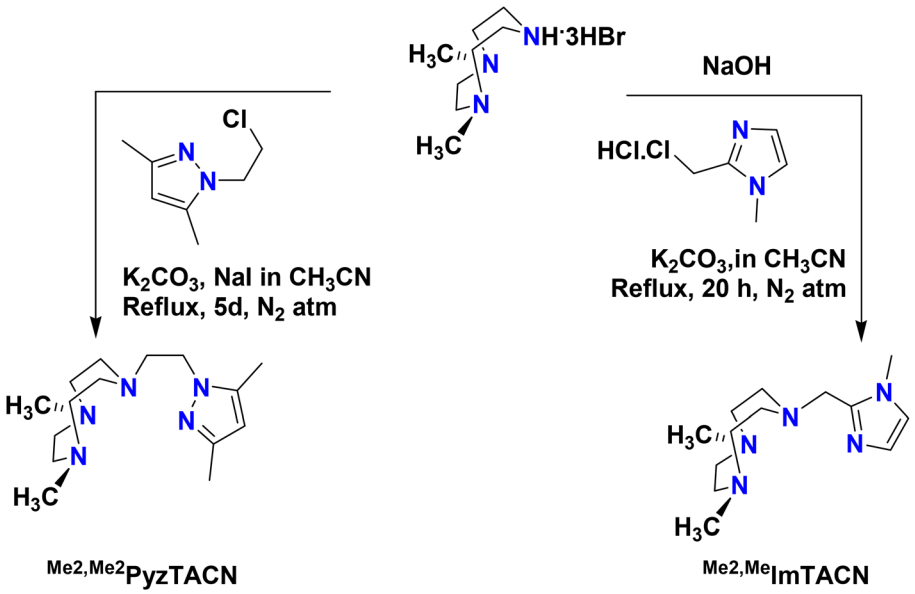

Scheme 3 Schematic synthetic routes to the ligands ^{Me2,Me2}**PyzTACN** and ^{Me2,Me}**ImTACN**. The free base 1,4-dimethyl-1,4,7-triazacyclononane was used for the synthesis of ^{Me2,Me2}**PyzTACN**.

Open Access Article. Published on 05 January 2023. Downloaded on 11/6/2025 11:33:04 PM.
This article is licensed under a Creative Commons Attribution 3.0 Unported Licence.

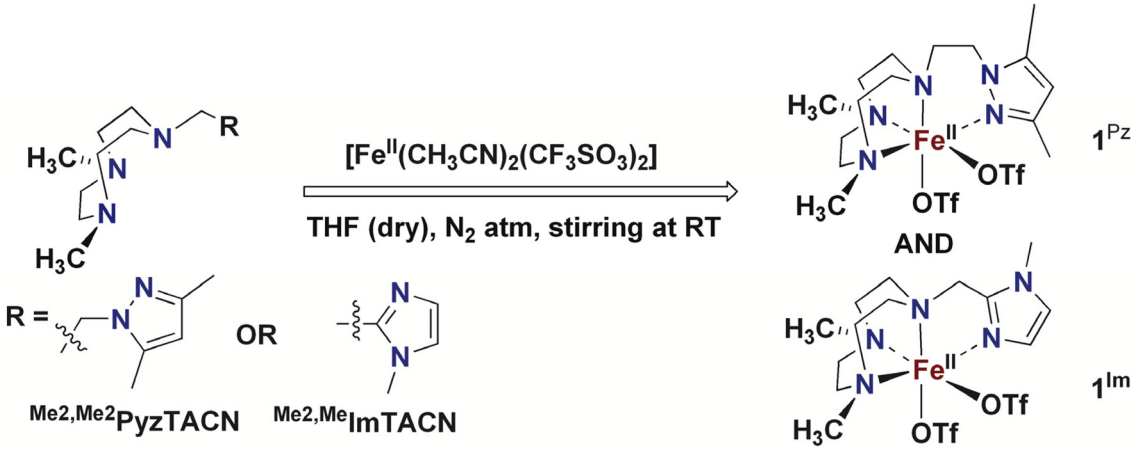

Scheme 4 Synthesis of Fe(II) complexes $\mathbf{1^{Pz}}$ and $\mathbf{1^{im}}$.

dried under vacuum (*cf.* Experimental section for a detailed description of the synthesis). The corresponding reaction with the $^{\mathbf{Me2,Me}}$**ImTACN** ligand in dry THF led to the formation of a complex that mostly remained in solution. The reaction solution was evaporated under vacuum and a small amount of a $CH_2Cl_2:CH_3CN$ (4 : 1) mixture was added to the resultant residue. Diffusion of diethyl ether into the resultant solution resulted in precipitation of the complex [Fe^{II}($^{\mathbf{Me2,Me}}$**ImTACN**)(CF_3SO_3)$_2$] ($\mathbf{1^{Im}}$, Scheme 4).

The complexes $\mathbf{1^{Pz}}$ and $\mathbf{1^{Im}}$ were characterized by mass spectrometry and ^{1}H NMR spectroscopy. The high resolution mass spectrum (HRMS) of $\mathbf{1^{Pz}}$ in CH_3CN showed prominent mass peaks at m/z = 167.5903 and 484.1303, corresponding to the formulations [Fe^{II}($^{\mathbf{Me2,Me2}}$**PyzTACN**)]$^{2+}$ (calc. 167.5881) and [Fe^{II}($^{\mathbf{Me2,Me2}}$**PyzTACN**)(CF_3SO_3)]$^+$ (calc. 484.1287), respectively (Fig. S1–S3, ESI†). Analogously, the HRMS of complex $\mathbf{1^{Im}}$ in CH_3CN showed prominent mass peaks at m/z = 153.5751 and 456.0970, corresponding to the formulations [Fe^{II}($^{\mathbf{Me2,Me}}$**ImTACN**)]$^{2+}$ (calc. 153.5724) and [Fe^{II}($^{\mathbf{Me2,Me}}$**ImTACN**)(CF_3SO_3)]$^+$ (calc. 456.0974), respectively (Fig. S4–S6†). The ^{1}H NMR spectra of the two complexes were measured in CD_3CN solvent (*cf.* Fig. S7 and S8†). Both complexes gave broad paramagnetically shifted spectra in spectral windows ranging from −10 to 120 ppm, indicative of the presence of high spin ferrous ions.

In order to confirm its identity, the solid-state structure of $\mathbf{1^{Pz}}$ was established by X-ray crystallography. The details of the structure determination are collated in Table S1 (ESI†). The X-ray structure (Fig. 2) shows that the Fe(II) center is in a slightly distorted octahedral coordination geometry. The ligand $^{\mathbf{Me2,Me2}}$**PyzTACN** is tetradentate with the three nitrogens of the triazacyclononane ring bound facially to the metal center and the pyrazole ring providing a fourth coordinated nitrogen. The two triflate anions are coordinated in *cis* positions on the Fe(II) ion. The Fe–N bond distances lie in the range 2.2–2.25 Å, which are typical distances observed for high spin Fe(II) complexes.[22–26] The Fe–O_{OTf} bond distances are 2.088(3) and 2.199(3) Å. In order to ensure that coordination of

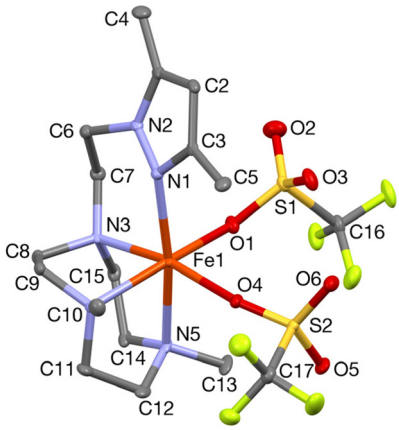

Fig. 2 A Mercury plot of the crystal structure of complex [Fe^{II}($^{\mathbf{Me2,Me2}}$**PyzTACN**)(CF_3SO_3)$_2$] ($\mathbf{1^{Pz}}$) with 50% probability ellipsoids. The hydrogens have been omitted for clarity. Selected bond distances (Å) and bond angles (°): Fe(1)–N(1) 2.209(3), Fe(1)–O(1) 2.088(3), Fe(1)–N(3) 2.227(4), Fe(1)–O(4) 2.199(3), Fe(1)–N(4) 2.208(4), Fe(1)–N(5) 2.249(3), N(1)–Fe(1)–N(5) 171.0(1), O(1)–Fe(1)–N(4) 166.7(1), N(3)–Fe(1)–O(4) 169.1(1).

the pyrazole nitrogen would be geometrically possible, the $^{\mathbf{Me2,Me2}}$**PyzTACN** ligand was designed to contain an ethylene spacer between the TACN ring and the pyrazole moiety, distinguishing this ligand from the related ligands discussed here, all of which contain methylene spacers in the corresponding positions. The Fe–N (pyrazole) bond distance is 2.209 (3) Å while the Fe–N(pyridine) bond distance is 2.165(4) Å in [Fe^{II}(^{Me,H}PyTACN)(CF_3SO_3)$_2$] ($\mathbf{1^{Py}}$)[16] and 2.246(2) Å in [Fe^{II}(^{Me,Me}PyTACN)(CF_3SO_3)$_2$] ($\mathbf{1^{MePy}}$),[27] and the Fe–N (benzimidazole) bond distance is 2.134(7) Å in [Fe^{II}($^{\mathbf{Me2,Me}}$**BzImTACN**)(CF_3SO_3)$_2$] ($\mathbf{1^{BzIm}}$).[21] The $_{OTf}$O–Fe–O_{OTf} angle is larger in $\mathbf{1^{Pz}}$ (93.6(1)°) than that of $\mathbf{3^{OTf}}$ (91.64(14)°)[16] and $\mathbf{1^{BzIm}}$ (89.1(3)°),[21] but shorter than that of $\mathbf{1^{MePy}}$ (94.9(7)°),[27] implying different steric environments around the Fe(II) center. It should be noted that one of the methyl groups of the pyrazole moiety lies in the same plane as the oxygen of one triflate anion (O4) and

Open Access Article. Published on 05 January 2023. Downloaded on 11/6/2025 11:33:04 PM.
This article is licensed under a Creative Commons Attribution 3.0 Unported Licence.

thus also in a plane roughly perpendicular to the iron-oxygen axis of the second triflate anion (*cf.* Fig. 2).

Catalytic C–H bond oxidation studies

The catalytic properties of $\mathbf{1^{Pz}}$ and $\mathbf{1^{Im}}$ were tested in the hydroxylation of several alkanes employing H_2O_2 as the oxidant. In a typical catalytic experiment, 10 equiv. of H_2O_2 (from a stock solution of 70 mM H_2O_2 in CH_3CN) were delivered by a syringe pump to a CH_3CN solution containing the Fe(II) complex (1 mM), alkane substrate (1 M) and H_2O (1 M) over a period of 30 min. The catalysis experiments were performed under air at room temperature. Under these conditions, both complexes oxidized cyclohexane into cyclohexanol ($\mathbf{1^{Pz}}$: TON 6.5; $\mathbf{1^{Im}}$: TON 7.7) as the main product with high alcohol/ketone (A/K) ratios ($\mathbf{1^{Pz}}$: A/K 9.4; $\mathbf{1^{Im}}$: 12) and high conversions of the oxidant (H_2O_2) into products ($\mathbf{1^{Pz}}$: 72%; $\mathbf{1^{Im}}$: 83%). Such high conversions and high A/K ratios are comparable to those obtained with related iron complexes under analogous experimental conditions.[16,21,25–31] The catalytic efficiencies of these two complexes with different alkane substrates are summarized in Table 1.

The high A/K ratios observed for these complexes suggest the involvement of a metal-based oxidant, as proposed previously.[32] Several other mechanistic substrate probes were used to verify the involvement of a metal-based active oxidant. The kinetic isotope effect (KIE) values obtained in the oxidation of a mixture of cyclohexane and its deuterated isotopologue (1 : 3 molar ratio) were 4.0 for $\mathbf{1^{Pz}}$ and 4.6 for $\mathbf{1^{Im}}$. Both of the complexes showed a preference for oxidation of tertiary C–H bonds over secondary C–H bonds in the oxidation of adamantane (normalized 3°/2° ratios were 12 for $\mathbf{1^{Pz}}$ and 26 for complex $\mathbf{1^{Im}}$). Finally, in the oxidation of *cis*-1,2-dimethylcyclohexane (*cis*-DMCH), the complexes provided the corresponding tertiary alcohol with a high degree of stereoretention (RC 83% for $\mathbf{1^{Pz}}$ and 100% for $\mathbf{1^{Im}}$), excluding any significant involvement of long-lived carbon-centered radicals or cations in the C–H oxidation reactions.

Isotope labelling studies

Isotope labelling experiments were performed using $H_2{}^{18}O_2$ and $H_2{}^{18}O$ to gain insight into the hydroxylation mechanism by determining the origin of the oxygen atom incorporated into the (alcohol) products. In the oxidation of cyclohexane (1000 equiv.), using 10 equiv. H_2O_2 in the presence of 1000 equiv. of $H_2{}^{18}O$ (Table 2), $\mathbf{1^{Pz}}$ (1 equiv.) was found to introduce only <3% labelled oxygen into the alcohol product. The complementary experiment performed with reverse labelling, *i.e.* 10 equiv. $H_2{}^{18}O_2$ and 1000 equiv. H_2O resulted in an ^{18}O-label incorporation of 86% into the alcohol. It may thus be concluded that peroxide is the main source of oxygen in the alcohol product and only 11% of oxygen atoms are incorporated from air/water (according to the oxygen mass balance) for this specific hydroxylation reaction. In the oxidation of other alkane substrates containing secondary C–H bonds, complex $\mathbf{1^{Pz}}$ with 10 equiv. H_2O_2 and 1000 equiv. of $H_2{}^{18}O$ gave rise to similar low percentages of incorporated ^{18}O (from water) into the alcohol (3% for cyclohexane-d_{12} and cyclooctane).

On the other hand, $\mathbf{1^{Im}}$ gave rise to considerably greater incorporation of oxygen from water into the products. In the presence of 10 equiv. H_2O_2 and 1000 equiv. of $H_2{}^{18}O$, complex $\mathbf{1^{Im}}$ (1 equiv.) gave 39 and 43% ^{18}O-alcohols in the oxidation of cyclohexane and cyclooctane, respectively (Table 2). The complementary experiment with 10 equiv. $H_2{}^{18}O_2$ and 1000 equiv. H_2O resulted in the formation of 55% ^{18}O-cyclohexanol in oxidation of cyclohexane. Thus, for this complex, both peroxide and H_2O are the sources of oxygen in the alcohol products. Again, the lack of significant incorporation of oxygen atoms from air rules out the transient formation of long-lived carbon-centered radicals.

In the oxidation of tertiary C–H bonds (*cis*-DMCH and adamantane), $\mathbf{1^{Pz}}$ did not incorporate any oxygen from water into the products (*cf.* Table 2). On the other hand, the equivalent experiments with $\mathbf{1^{Im}}$ led to 39% and 31% oxygen incorporations from water into product(s) in the oxidation of adamantane and *cis*-DMCH, respectively (*cf.* Table 2). For comparison, results from oxidation with structurally related catalysts are included in Table 2.

cis-Dihydroxylation *vs.* epoxidation in the oxidation of alkenes

Complexes $\mathbf{1^{Pz}}$ and $\mathbf{1^{Im}}$ catalyzed the oxidation of alkenes in the presence of H_2O_2 and H_2O to give both epoxide and *cis*-dihydroxylated products. Under catalytic conditions (1 : 10 : 1000 for catalyst : oxidant : substrate), $\mathbf{1^{Pz}}$ oxidized *cis*-cyclooctene to give *cis*-cyclooctene epoxide (TON 8.2) as a major product with the concomitant formation of a minor amount of *syn*-cyclooctane-1,2-diol (TON 0.5), *i.e.* an epoxide : diol (E/D) ratio of 16.5. Addition of H_2O (1000 equiv.) slightly increased the formation of *syn*-diol (TON 1.1), but had almost no influence in the yield of epoxide (TON 8.2). When 100 equiv. of H_2O_2 was employed, the yield of both epoxide (TON 53) and *cis*-diol (TON 4.8) was increased. In the oxidation of 1-octene, using 100 equiv. H_2O_2, $\mathbf{1^{Pz}}$ yielded 1-octene epoxide (TON 16.5) as the major product together with a minor amount of *syn*-dihydroxylated product (TON 2.5). Complex $\mathbf{1^{Im}}$, on the other hand, preferred formation of *syn*-diol over epoxide in the oxidation of *cis*-cyclooctene; in this reaction, complex $\mathbf{1^{Im}}$ (1 equiv.) together with H_2O_2 (10 equiv.) produced *syn*-cyclooctane-1,2-diol with a TON of 5.9 and *cis*-cyclooctene

Table 1 Catalytic C–H bond oxidation of various alkanes by Fe-complexes $\mathbf{1^{Pz}}$ and $\mathbf{1^{Im}}$, using H_2O_2

Catalyst	Substrate	TN (A)	TN (K)	A/K	Yield (%)
$\mathbf{1^{Pz}}$	Cyclohexane	6.5	0.7	9.3	72
$\mathbf{1^{Im}}$	Cyclohexane	7.7	0.64	12	83
$\mathbf{1^{Pz}}$	Cyclohexane-d_{12}	4	0.5	8	45
$\mathbf{1^{Im}}$	Cyclohexane-d_{12}	5	0.5	10	55
$\mathbf{1^{Pz}}$	Cyclooctane	6	0.6	10	66
$\mathbf{1^{Im}}$	Cyclooctane	6.2	0.6	10.3	69
$\mathbf{1^{Pzf}}$	*n*-Hexane	3	0.8	3.8	38
$\mathbf{1^{Im}}$	*n*-Hexane	3.6	0.64	5.6	43
$\mathbf{1^{Pz}}$	2,3-Dimethylbutane	2.6	—	—	26
$\mathbf{1^{Im}}$	2,3-Dimethylbutane	3.5	—	—	35

 This journal is © The Royal Society of Chemistry 2023

Open Access Article. Published on 05 January 2023. Downloaded on 11/6/2025 11:33:04 PM.
This article is licensed under a Creative Commons Attribution 3.0 Unported Licence.

Table 2 ^{18}O incorporation from $H_2{}^{18}O$ in C–H hydroxylation reactions mediated by different Fe(II) complexes. [a]Unless explicitly stated, reactions were conducted under air

Substrate	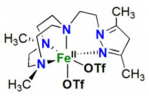 $\mathbf{1^{Pz}}$	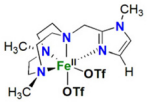 $\mathbf{1^{Im}}$	$\mathbf{1^{Py}}$[e]	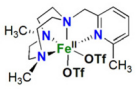 $\mathbf{1^{MePy}}$[e]	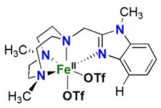 $\mathbf{1^{BzIm}}$[f]
Cyclohexane	3 1[c] 11[d]	39 36[c] 3[d]	45	11	48
Cyclohexane-d_{12}	3	NA	40	NA	48
Cyclooctane	3	43	44	NA	41
cis-DMCH	0	31	79	2	26
Adamantane	0	39	74	3	28
cis-Cyclooctene[b] epoxide	2 11[d]	36 36[c] 8[d]	77	5	24
syn-Cyclooctane-1,2-diol[b]	97 4[d]	92 91[c] 3[d]	97	78	98

[a] Reaction conditions: catalyst : H_2O_2 : $H_2{}^{18}O$: substrate = 1 : 10 : 1000 : 1000, CH_3CN, RT, air. [b] *cis*-Cyclooctene was employed as the substrate. [c] Reaction performed under N_2. [d] Catalyst : H_2O_2 : H_2O : substrate = 1 : 10 : 1000 : 1000, CH_3CN, RT, under $^{18}O_2$. [e] ref. 16–18,20. [f] ref. 21.

epoxide with a TON of 3.9 (E/D = 0.6) and an overall conversion of 96% (w.r.t. the oxidant). In the oxidation of the terminal alkene 1-octene, complex $\mathbf{1^{Im}}$ (1 equiv.) together with H_2O_2 (10 equiv.) produced *cis*-diol with a TON of 4.4 and epoxide with a TON of 1.5 (E/D = 3) and a conversion of approximately 36%.

In order to investigate the identity of the active oxidant, isotope labelling studies were made for both complexes, employing *cis*-cyclooctene as substrate. In the presence of 10 equiv. H_2O_2 and 1000 equiv. $H_2{}^{18}O$, $\mathbf{1^{Pz}}$ (1 equiv.) introduced 97% (100% and 200% account for one and two ^{18}O atoms per diol product, respectively) ^{18}O into the product *syn*-cyclooctane-1,2-diol during the oxidation of *cis*-cyclooctene, while complex $\mathbf{1^{Im}}$ gave 92% label incorporation under the same conditions. These results are in full agreement with previous isotope labelling results on the Fe(**PyTACN**) family of complexes and of the related complex [Fe($^{\mathbf{Me2,Me}}$**BzImTACN**)(OTf)$_2$], $\mathbf{1^{BzIm}}$.[21] This isotopic labelling pattern is indeed a distinctive feature of the so called class I type of iron catalysts.[18] These catalysts are proposed to operate *via* a high valent $Fe^{V}(O)(OH)$ active species, formed *via* water assisted O–O cleavage of an $Fe^{III}(OOH)(OH_2)$ precursor.[19] In accordance with this scheme, *syn*-dihydroxylation of olefins by $Fe^{V}(O)(OH)$ results in diols where one of the two oxygen atoms originates from water and the other from hydrogen peroxide. Consequently, the isotopic labelling data derived from the *syn*-dihydroxylation reactions (Table 2) indicate that the series of complexes $\mathbf{1^{Pz}}$, $\mathbf{1^{Im}}$, $\mathbf{1^{BzIm}}$, $\mathbf{1^{Py}}$ and $\mathbf{1^{MePy}}$ can all be categorized as class I type of iron catalysts, operating *via* a $Fe^{V}(O)(OH)$ species.

On the other hand, the epoxidation reaction presents a completely different pattern to the *syn*-dihydroxylation. The isotopic labelling in the epoxidation actually parallels the alkane hydroxylation reaction, a similarity that may be attributed to the fact that in these reactions only the oxygen atom of the oxo ligand is transferred to the substrate, while the hydroxide ligand remains in the complex. Thus, interrogation of the ^{18}O labelling in the epoxidation reaction may be used to establish the origin of the oxygen atoms in the reactive oxo ligand.

Interestingly, when the incorporation of water into *cis*-cyclooctene epoxide was analyzed, complex $\mathbf{1^{Pz}}$ behaved drastically different from $\mathbf{1^{Im}}$. The incorporation of ^{18}O using $H_2{}^{18}O$ was 36% for the latter, while only ~2% for the former. For comparison, for the related complexes $\mathbf{1^{BzIm}}$ and $\mathbf{1^{Py}}$, the amount of ^{18}O-labeled epoxides formed were 24 and 77%, respectively. Therefore, the origin of the oxo ligand differs in a substantial manner in the series of complexes from $\mathbf{1^{Pz}}$, where the oxo ligand originates from H_2O_2 in a practically quantitative manner, to $\mathbf{1^{Py}}$ where it predominantly (77%) originates from water. We thus conclude that the incorporation of water in the reactive oxo ligand differs substantially within the series of complexes. It may be noted that the chemoselectivity patterns and the isotopic labelling data collated in Tables 1 and 2 for the five catalysts are not consistent with reactions where $Fe^{IV}(O)$ species are the main oxidants.[16–18,21,24,33–37]

Finally, control experiments were conducted to investigate the possible involvement of O_2 from air in the reactions. The O-inventory in the reactions catalyzed by $\mathbf{1^{Py}}$, $\mathbf{1^{MePy}}$ and $\mathbf{1^{BzIm}}$ has been studied previously by performing oxidation reactions with ^{18}O-labelled peroxide and water, under air. In these reactions it was shown that the oxygen atoms in the oxidized products are derived from the peroxide or water and that atmospheric oxygen atoms account for <10% of incorporated oxygen.[16,18,21] In order to address the possible implication of O_2 in the reactions of $\mathbf{1^{Pz}}$ and $\mathbf{1^{Im}}$, the following experiments were performed, the results of which are included in Table 2; – oxidation of cyclohexane with $\mathbf{1^{Pz}}$ was performed under a N_2 atmosphere and also under an $^{18}O_2$ atmosphere. The data

Open Access Article. Published on 05 January 2023. Downloaded on 11/6/2025 11:33:04 PM.
This article is licensed under a Creative Commons Attribution 3.0 Unported Licence.

show no significant changes between air and N_2 atmospheres and a small (11%) incorporation of oxygen from $^{18}O_2$ in the C–H oxidation. Oxidation of cyclooctene with $\mathbf{1^{Pz}}$ was also performed under $^{18}O_2$ and the data were compared with reactions performed under air. The epoxide shows a small incorporation of ^{18}O from $^{18}O_2$ (11%), resembling the C–H oxidation reaction. However, the *cis*-diol shows no significant incorporation of ^{18}O from $^{18}O_2$. It can be concluded that O_2 participates to a minor extent in the epoxidation and C–H hydroxylation reaction, but not in the *cis*-dihydroxylation.

Oxidation of cyclohexane with $\mathbf{1^{Im}}$ was performed under a N_2 atmosphere and also under an $^{18}O_2$ atmosphere. The data shows no significant changes between air and N_2 atmospheres and marginal (3%) incorporation of oxygen from $^{18}O_2$ in the C–H oxidation. Oxidation of cyclooctene with $\mathbf{1^{Pz}}$ was then performed under $^{18}O_2$, under N_2 and the data were compared with reactions performed under air. The epoxide shows a small incorporation of ^{18}O from $^{18}O_2$ (8%). However, as was the case for $\mathbf{1^{Im}}$, the *cis*-diol shows again no significant incorporation of ^{18}O from $^{18}O_2$. We conclude again that in the catalytic oxidations conducted using $\mathbf{1^{Im}}$ as a (pre)catalyst, only a minor extent of O_2 participation is detected in the epoxidation reaction but not in the *cis*-dihydroxylation and C–H hydroxylation reactions. Overall, the data indicate that atmospheric O_2 is either not implicated in the reactions, or represents only a minor pathway in the epoxidation reactions for both catalysts, and in the C–H hydroxylation catalyzed by $\mathbf{1^{Pz}}$.

In summary, the very minor involvement of O_2 in the reactions is consistent with the mechanistic interpretation for the C–H and C=C oxidation reactions detailed above, where a metal based $Fe^{V}(O)(OH)$ oxidant is responsible for substrate oxidation. Radical intermediates must be short lived and react within the solvent cage.

It should be borne in mind that intramolecular C–H bond activation/ligand oxidation in the course of the above-mentioned oxidation reactions cannot be ruled out, but such reactions were not specifically studied. Mass spectrometric measurements did not provide any evidence of such side reactions.

Computational modelling

In order to gain an understanding of the relative energies of the postulated $Fe^{V}(O)(OH)$ tautomers, computational modelling of the two tautomers generated from $[Fe^{II}(^{Me2,Me}\mathbf{BzImTACN})(CF_3SO_3)_2]$ ($\mathbf{1^{BzIm}}$)[21] was undertaken. The ground-state stability ordering of the two ^{Me2,Me}BzIm compounds was computationally investigated by density functional theory (DFT), the tautomeric species were labelled in accordance with Scheme 2, *i.e.* the species that contains an oxo moiety coplanar with the benzimidazole ligand is labelled as $\mathbf{O_A}$, while $\mathbf{O_B}$ represents the isomer whose oxo moiety is perpendicular to the heterocyclic ligand (Fig. 3). The DFT analyses confirm the quartet state (S = 3/2) as the thermodynamically favoured spin state for both isomers, with $^4\mathbf{O_A}$ found to lie 2.4 kcal mol^{-1} lower in energy than $^4\mathbf{O_B}$. The locus of the unpaired spin density in both tautomers is similar, and the largest contributions of unpaired spin populations (Fig. 3) are found on the iron and oxo oxygen atoms. Interestingly, each tautomer displays a small amount of spin density at the hydroxyl oxygen atom.

The corresponding doublet spin states of $^2\mathbf{O_A}$ and $^2\mathbf{O_B}$ (S = 1/2) lie 11.5 and 9.1 kcal mol^{-1} higher in energy than their respective quartet counterparts. Having established the ground-state stability ordering and spin-state preference for the two isomeric oxo-hydroxyl compounds, the lability of proton transfer between these tautomers was next explored. Proton transfer between the different oxygen centers in $^4\mathbf{O_A}$ and $^4\mathbf{O_B}$ occurs through transition structure $^4\mathbf{TS}^4\mathbf{O_A}^4\mathbf{B}$, as depicted in Fig. 4, and basically involves the synchronous transfer of the hydrogen between the two oxygen centers. The free-energy barrier is high and in excess of 30 kcal mol^{-1}, and these data are in keeping with the reported configurational stability of the related pyridyl-derivatives prepared by Company and Costas.[18] The absence of facile proton transfer between the two oxygen centers in $^4\mathbf{O_A}$ and $^4\mathbf{O_B}$ suggests that the oxo-based C–H abstractions observed in these studies must originate from structurally different oxidants that do not allow equilibration of the oxo moiety on the time scale of the chemi-

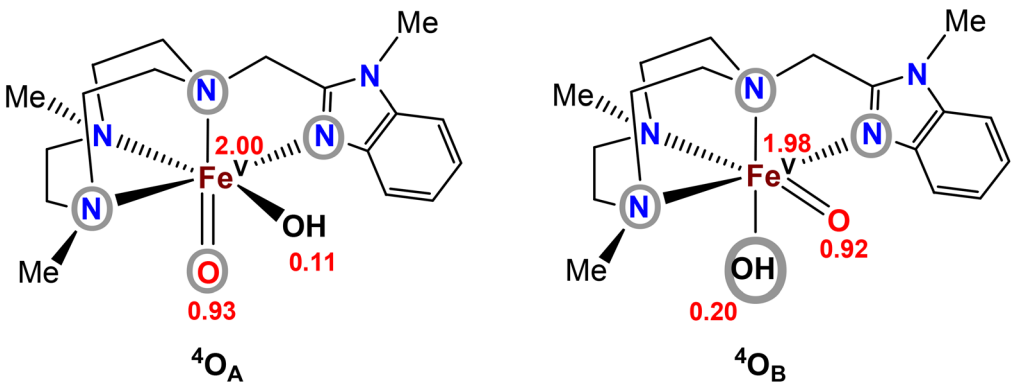

Fig. 3 Computed spin-density populations in the two tautomers of complex $\mathbf{2^{BzIm}}$ (*cf.* Scheme 2). Atoms/groups inside grey circles indicate the ligand entities that lie in the equatorial planes of the tautomers.

Open Access Article. Published on 05 January 2023. Downloaded on 11/6/2025 11:33:04 PM.
This article is licensed under a Creative Commons Attribution 3.0 Unported Licence.

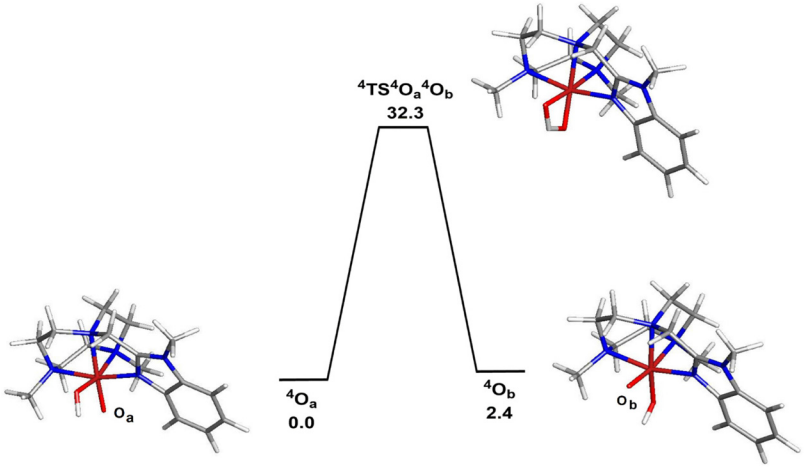

Fig. 4 B3LYP-optimized structures and potential energy surface for the isomerization of ^4O_A (^{4}A) to ^4O_B (^{4}B). Energy values are in ΔG in kcal mol^{-1} relative to ^4O_A.

cal reactions, a feature supported by the isotopic labelling studies.

In order to elucidate the mechanism of the hydrogen-atom transfer (HAT) of alkanes by $^4\mathbf{O_A}$ and $^4\mathbf{O_B}$, DFT calculations were carried out using methane (C) as the substrate.[38] This particular substrate was chosen in order to simplify the calculations and reduce the computational time. Fig. 5 shows the geometry-optimized transition-state structures involved in the H-abstraction and the resulting MeOH-substituted compounds, while Fig. 6 shows the potential energy surface for these reactions. Hydrogen abstraction is mediated by the oxo moiety in $^4\mathbf{O_A}$ and $^4\mathbf{O_B}$, leading to the respective transition-state structures $^4\mathbf{TS^4O_AC^6D}$ and $^4\mathbf{TS^4O_BC^6E}$, which lie 25.1 and 22.9 kcal mol^{-1}, respectively, above the pertinent tautomer and methane reactants. The transition state for methane activation from the less stable tautomer lies 2.2 kcal mol^{-1} lower in energy from the corresponding transition state $^4\mathbf{TS^4O_AC^6D}$ formed from the thermodynamically favoured tautomer ^{4}**A**. The expected geminate radical pairs that follow each H-abstraction could not be found by IRC calculations, presumably a manifestation of the flat nature of the reaction surface *en route* to the alcohol product. Collapse of the geminate radical pair in each reaction *via* a rebound process, coupled with a spin crossover to the thermodynamically favoured high-spin sextet species (S = 5/2), completes the hydroxylation sequence and affords the MeOH-substituted products ^{6}**D** and ^{6}**E**. Both hydroxylation routes are exergonic in nature, and the MeOH-substituted product having the alcohol ligand disposed perpendicular to the heterocyclic ligand is more stable (by a 3.1 kcal mol^{-1}) due to reduced interactions between the coordinated alcohol and ligand scaffold.

The same calculations were carried out for $\mathbf{2^{Im}}$ and $\mathbf{2^{Pz}}$. For both complexes, the $\mathbf{O_B}$ tautomer is the least favoured (by 1.4 kcal mol^{-1} for $\mathbf{2^{Im}}$, and by 3.7 kcal mol^{-1} for $\mathbf{2^{Pz}}$). Furthermore, in agreement with the results obtained for $\mathbf{2^{BzIm}}$ that are discussed above, HAT from methane is favoured for this least stable tautomer with a transition state that is stabilized by 2.5 kcal mol^{-1} for $\mathbf{2^{Im}}$ (21.9 *vs.* 24.4 kcal mol^{-1}) and by 4.9 kcal mol^{-1} for $\mathbf{2^{Pz}}$ (29.3 *vs.* 24.4 kcal mol^{-1}) (*cf.* ESI†). Overall, a general trend in relative energy between the isomers was observed. In all three cases, the computed ground state energy for $\mathbf{O_B}$ lies higher than that for $\mathbf{O_A}$. This trend can be rationalized by considering that the iron coordination site coplanar with the heterocycle is sterically more congested, as rapidly deduced from an inspection of the two coordination sites in Fig. 3. Presumably, the higher steric demand of the OH ligand when compared with the terminal oxo, arising from the larger Fe–O(H) distance, destabilizes isomer $\mathbf{O_B}$, where the hydroxide and the heterocycle are coplanar. The more stable isomer $\mathbf{O_A}$ thus contains the reactive oxo ligand buried in the sterically more congested site, which may disfavour reaction against an external substrate. Furthermore, $\mathbf{O_B}$ is relatively more destabilized for $\mathbf{2^{Pz}}$ when compared to $\mathbf{2^{BzIm}}$ and $\mathbf{2^{Im}}$; the order of this relative destabilization is $\mathbf{2^{Pz}} > \mathbf{2^{BzIm}} > \mathbf{2^{Im}}$, in keeping with the relative steric hindrance for the three ligands. In addition, the computed HAT profiles for the three complexes (Fig. 6 and ESI†) show that the relative stabilization in the HAT reaction, going from the transition state for $\mathbf{O_A}$ ($^4\mathbf{TS^4O_AC^6D}$, *cf.* Fig. 6) to the more favoured transition state for $\mathbf{O_B}$ ($^4\mathbf{TS^4O_BC^6D}$) also follows the order $\mathbf{2^{Pz}} > \mathbf{2^{BzIm}} > \mathbf{2^{Im}}$. The calculations thus indicate that the least stable tautomer is also the most reactive against the C–H bond, but differences in energy are relatively small and may be dependent on computational details. Consequently, the calculations support the idea that both isomers can participate in the oxidation reactions. A perspective analysis of the results from the computations and the experimental data suggest that indeed the observed outcome in the isotopic labelling experiments reflects the relative participation of the two tautomers in the catalytic oxidation reactions, which in turn result from a balance between their relative ground state energies, and their relative reactivities toward C–H and C=C bonds (activation energies).

Open Access Article. Published on 05 January 2023. Downloaded on 11/6/2025 11:33:04 PM.
This article is licensed under a Creative Commons Attribution 3.0 Unported Licence.

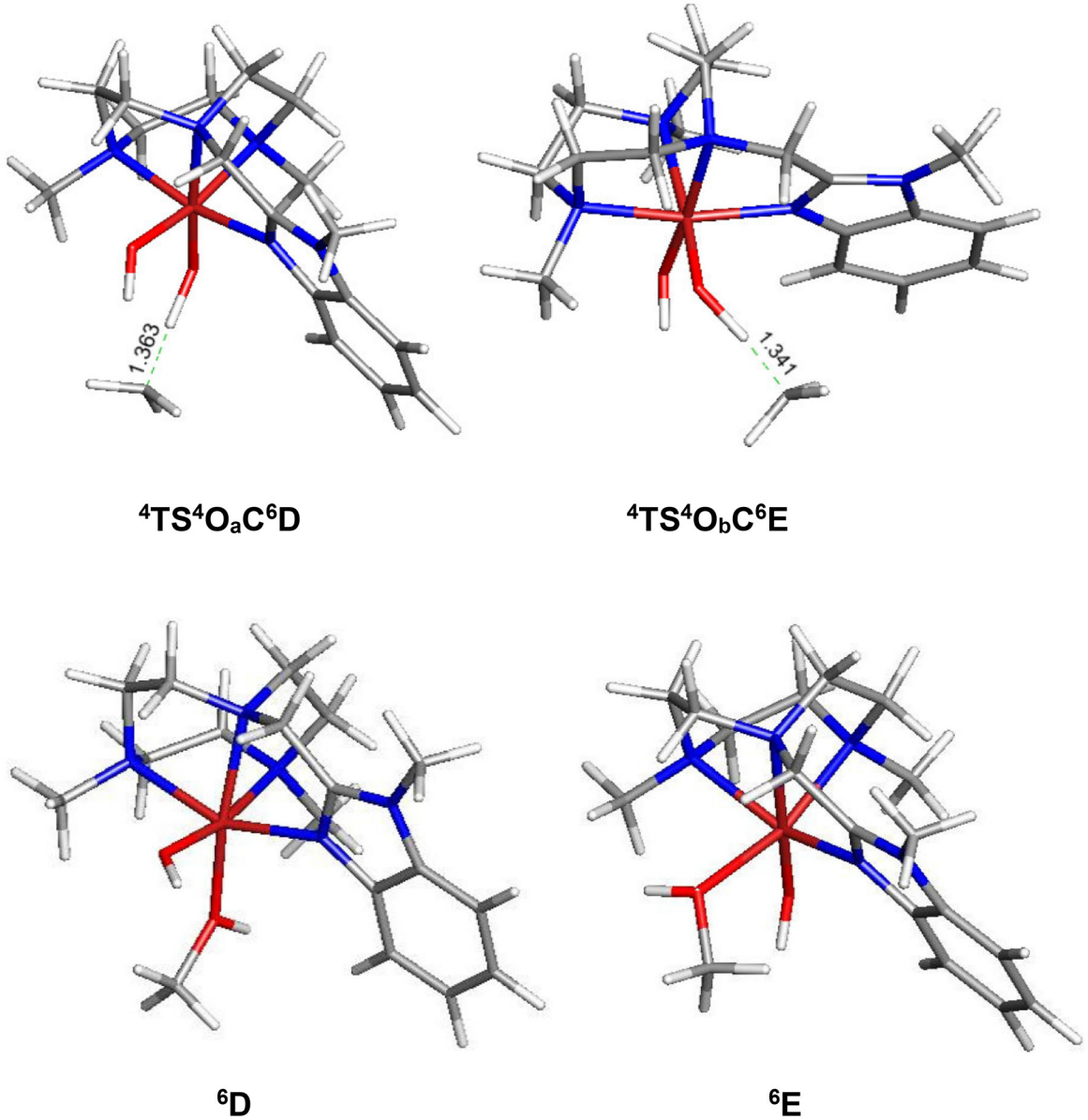

Fig. 5 B3LYP-optimized transition structures $^4TS^4O_aC^6D$ and $^4TS^4O_bC^6E$ and the MeOH-substituted products ^6D and ^6E from methane (C) hydroxylation reaction using ^4O_a and ^4O_b.

Summary and conclusions

We have previously demonstrated the steric influence exerted by ligands on the relative reactivities of iron(v) oxo-hydroxo tautomers operating in C–H hydroxylation reactions.[21] This study further addresses and strengthens the fact that the ligand exerts a profound influence on the relative oxygen atom transfer reactivity, with the steric bulk of the donor moiety of the pendant arm attached to the TACN ligand deciding the relative ease of approach of a substrate towards the reactive oxo-ligand at position A (*trans* to **N**-CH_2R, tautomer $\mathbf{O_A}$) or at position B (*trans* to a **N**-Me, tautomer $\mathbf{O_B}$) of the proposed active Fe(v)(O)(OH) oxidant. An inspection of the space-filling diagrams generated for the series of complexes $\mathbf{2^{Py}}$, $\mathbf{2^{MePy}}$, $\mathbf{2^{Im}}$, $\mathbf{2^{BzIm}}$, and $\mathbf{2^{Pz}}$ (*cf.* Fig. 7) shows that position A is sensitive to the nature of the ligand heterocycle. The crystal structures of the Fe(ii) catalysts, which are direct precursors to the active perferryl ($Fe^V(O)$) oxidants, provide a structural basis for the steric influence of the ligands.

As illustrated in Fig. 7, the oxygen atom that lies in the N_3-donor plane of the ligand(s) in which the "pendant" N-donor ligand is situated (*i.e.* corresponding to the oxo ligand in tautomer $\mathbf{O_A}$, *cf.* Fig. 3) is positioned in a sterically more encumbered environment than the oxygen atom in the $\mathbf{O_B}$ position, which protrudes from the ligand plane. On steric grounds, it may therefore be expected that sterically hindered C–H entities, *e.g.* tertiary C–H bonds, will react preferentially with the least sterically hindered oxygen atom/oxido ligand, *i.e.* that of

 This journal is © The Royal Society of Chemistry 2023

Open Access Article. Published on 05 January 2023. Downloaded on 11/6/2025 11:33:04 PM.
This article is licensed under a Creative Commons Attribution 3.0 Unported Licence.

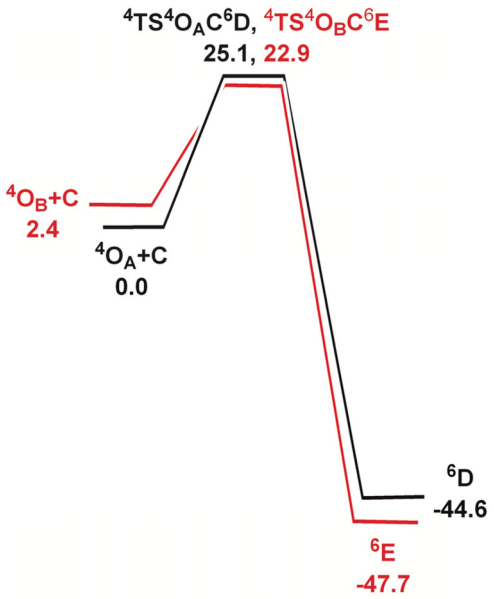

Fig. 6 Potential energy surface for the reaction of ^{4}O$_A$ and ^{4}O$_B$ with methane (**C**). Energy values are in ΔG in kcal mol^{-1} relative to the respective Fe(oxo)(hydroxo) tautomer and **C**.

the $\mathbf{O_B}$ tautomer. As there is evidence that the oxo ligand in $\mathbf{O_A}$ originates from water,[18,19] the relative incorporation of oxygen from $H_2{}^{18}O$ into a (sterically bulky) alkane substrate (especially those containing tertiary C–H bonds) may be used as a guide to the steric influence of the ligand on substrate access to the $\mathbf{O_A}$ oxo ligand – low incorporation of labelled oxygen into the oxidation product indicates steric hindrance by the ligand. The levels of incorporation of ^{18}O from water into the substrates (cyclohexane, cyclooctane, adamantane, *cis*-DMCH, *cis*-cyclooctene) are listed in Table 2. For complex $\mathbf{1^{Pz}}$, the very low percentage of ^{18}O incorporation (<3%) from $H_2{}^{18}O$ in the products suggests that the $\mathbf{O_B}$ tautomer predominates over $\mathbf{O_A}$ (irrespective of substrates containing secondary or tertiary C–H bonds) in the C–H hydroxylation reaction. On the other hand, the levels of ^{18}O incorporation (within the range 30–45%) from $H_2{}^{18}O$ into products for complex $\mathbf{1^{Im}}$ indicate that both $\mathbf{O_A}$ and $\mathbf{O_B}$ are equally reactive towards substrates with little preference of $\mathbf{O_B}$ over $\mathbf{O_A}$ for substrates containing tertiary C–H bonds.

While the high percentage (above 90%) ^{18}O incorporation in the *syn*-diol product in oxidation of *cis*-cyclooctene by complexes $\mathbf{1^{Pz}}$ and $\mathbf{1^{Im}}$ (*cf.* Table 2) demonstrates the involvement of Fe(v)(O)(OH) oxidant as observed for Fe(**PyTACN**) complexes, the different ranges of ^{18}O incorporation into the epoxide product also discriminate the relative reactivity between $\mathbf{O_A}$ and $\mathbf{O_B}$. The amounts of labelled epoxide were 2% and 36% for complexes $\mathbf{1^{Pz}}$ and $\mathbf{1^{Im}}$, respectively, clearly implying that epoxidation reaction catalyzed by complex $\mathbf{1^{Pz}}$ is performed exclusively by $\mathbf{O_A}$ and in complex $\mathbf{1^{Im}}$, $\mathbf{O_A}$ and $\mathbf{O_B}$ are active in an approximate 2/1 ratio.

On the basis of these experimental results, the order of steric interference of the ligand with the $\mathbf{O_A}$ oxo ligand (*cf.* Scheme 2 and Fig. 7) is $\mathbf{1^{Pz}} > \mathbf{1^{MePy}} > \mathbf{1^{BzIm}} > \mathbf{1^{Im}} > \mathbf{1^{Py}}$. Indeed, it is interesting to notice that the steric bulk inside the first coordination sphere of the different Fe(II) precursor complexes obtained from percent buried volume (%V_{bur})[39] calculations based on the crystallographic data for $\mathbf{1^{Pz}}$, $\mathbf{1^{MePy}}$, $\mathbf{1^{BzIm}}$ and $\mathbf{1^{Py}}$ follows the same order. Fig. 7 shows space filling models for the ligand pockets and the corresponding calculated %V_{bur} values for the crystal structures of $\mathbf{1^{Pz}}$, $\mathbf{1^{MePy}}$, $\mathbf{1^{BzIm}}$ and $\mathbf{1^{Py}}$ (*cf.* Experimental section and ESI† for details). There are no crystal data for $\mathbf{1^{Im}}$, but the percent buried volume for this complex is anticipated to lie between the values obtained for $\mathbf{1^{BzIm}}$ and $\mathbf{1^{Py}}$. The *N*-methyl imidazole ring has a sterically less pronounced effect on the metal center compared to the *N*-methyl benzimidazole ring in $\mathbf{1^{BzIm}}$, but has a higher steric effect compared to the pyridine ring present in $\mathbf{1^{Py}}$ (Fig. 8).

The results described above indicate that the steric bulk of the tetradentate TACN-based ligands exerts a significant influence on the relative HAT reactivities of the postulated tautomeric Fe^V(O)(O) oxidants. It should be noted that different

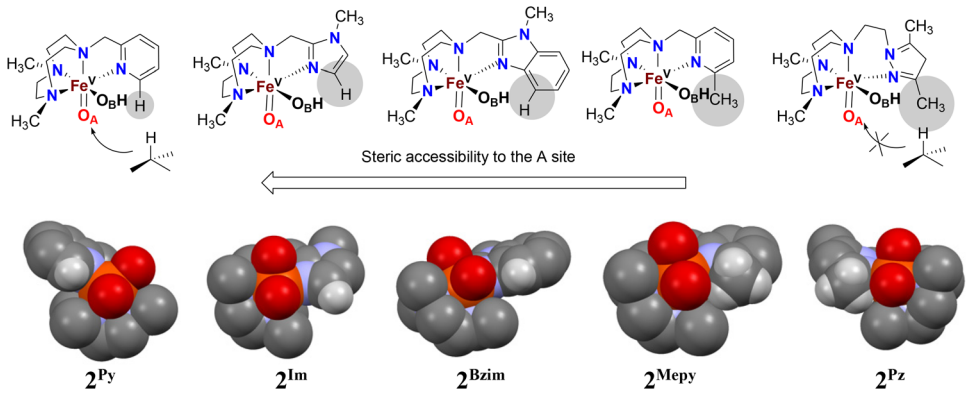

Fig. 7 Schematic depictions (top) and space filling models (bottom) of the Fe(v)(O)(OH) species $\mathbf{2^{Py}}$, $\mathbf{2^{Im}}$, $\mathbf{2^{BzIm}}$, $\mathbf{2^{MePy}}$, and $\mathbf{2^{Pz}}$ obtained by modifying the crystal structures of $\mathbf{1^{Py}}$, $\mathbf{1^{BzIm}}$, $\mathbf{1^{MePy}}$ and $\mathbf{1^{Pz}}$ by excluding most hydrogens and only displaying the oxygen atoms of the trifluoromethylsulfonate ligands. The space-filling structure of $\mathbf{2^{Im}}$ is derived from the structure of $\mathbf{1^{BzIm}}$, with the imidazolyl hydrogen being placed in the position benzimidazolyl carbon atom.

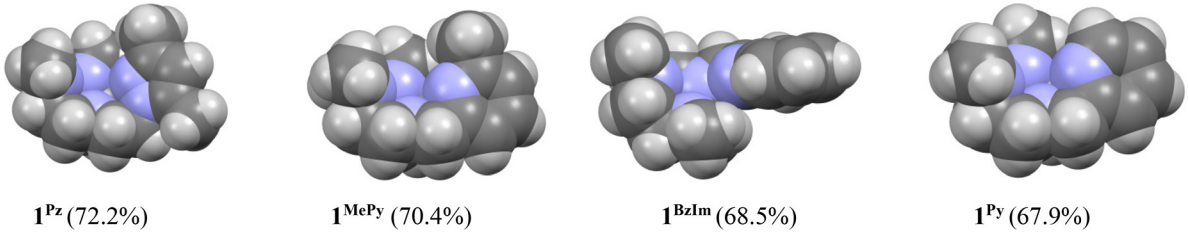

Fig. 8 Space filling models and the corresponding percent buried volume (%V_{bur}) values of the ligand pockets, within a 3.5 Å radius of the centrally located iron ion, in the Fe(II) precursor complexes $\mathbf{1}^{Pz}$, $\mathbf{1}^{MePy}$, $\mathbf{1}^{BzIm}$ and $\mathbf{1}^{Py}$.

Open Access Article. Published on 05 January 2023. Downloaded on 11/6/2025 11:33:04 PM.
This article is licensed under a Creative Commons Attribution 3.0 Unported Licence.

basicities or donor properties possessed by the side arms ((*N*-methyl)imidazole, (*N*-methyl)benzimidazole and 3,5-dimethylpyrazole) of the tetradentate ligands might have some influence on the reactivity of Fe(V)(O)(OH) oxidant in general, and the relative reactivities of the two tautomers in particular. However, the electronic effects of the side arms are not as apparent or conclusive as the steric properties of the side arms from the present investigation. Thus, the possible effects of electronic properties of the ligands on the reactivities need to be clarified, and further studies are undertaken towards this direction.

Experimental section

Reagents and materials

Reagents and solvents were of at least 99% purity and used as received without any further purification. $H_2{}^{18}O_2$ (90% ^{18}O-enriched, 2% solution in $H_2{}^{18}O$) and $H_2{}^{18}O$ (95% ^{18}O-enriched) were purchased from ICON isotopes. All reagents and solvents were purchased from Sigma Aldrich or Fisher Scientific. Dichloromethane and acetonitrile were dried by distillation from CaH_2; diethyl ether was dried by distillation from Na/benzophenone. The starting materials 1-(2-chloroethyl)-3,5-dimethyl-1*H*-pyrazole,[40] 1-(2-chloromethyl)-2-methylimidazole hydrochloride,[41] and 4,7-dimethyl-1,4,7-triazacyclononane[42] or its trihydrobromide salt[43] were synthesized according to literature procedures.

Instrumentation

Infrared spectra were collected on a Nicolet Avatar 360 FTIR spectrometer. UV-Visible spectroscopy was performed in a 1 cm quartz cell using an Agilent Technology 8453 UV-Vis spectrophotometer equipped with a diode-array detector. NMR spectra were recorded a Bruker DPX 400 MHz and Varian Inova 500 MHz spectrometers in $CDCl_3$ or CD_3CN solvent using standard conditions, and were referenced to the residual proton signal of the solvent. Elemental analysis was performed on a 4.1 Vario EL 3 elemental analyzer from Elementar. The ESI-MS experiments were performed with a Bruker Esquire 6000 LC/MS chromatograph, using acetonitrile as a mobile phase. The product analyses after catalysis experiments were carried out on an Agilent Technology 7820A gas chromatograph equipped with a 16-sample automatic liquid sampler, flame ionization detector and EzChrom Elite Compact software. GC-MS analyses were performed on an Agilent Technology 7890A GC system equipped with a 5975C inert XL EI/CI MSD with triple-axis detector. The products were identified by comparison of their GC retention times and, in the case of GC/MS, with those of authentic compounds.

Syntheses

Synthesis of ^{Me2,Me2}PyzTACN [1-(2-(3,5-dimethyl-1*H*-pyrazol-1-yl)ethyl)-4,7-dimethyl-1,4,7-triazacyclo-nonane]. A mixture of 1-(2-chloroethyl)-3,5-dimethyl-1*H*-pyrazole (243 mg, 1.53 mmol, 1.0 equiv.), 1,4-dimethyl-1,4,7-triazacyclononane (294 mg, 1.84 mmol, 1.2 equiv.), K_2CO_3 (1.27 g, 9.18 mmol, 6.0 equiv.), NaI (229 mg, 1.53 mmol, 1.0 equiv.) and Na_2SO_4 (435 mg, 3.06 mmol, 2.0 equiv.) in CH_3CN were stirred for 5 days at 90 °C under N_2 atmosphere. After cooling down to room temperature, the resultant mixture was filtered through a Celite pad, after which the Celite pad was washed with CH_2Cl_2 (40 ml). The filtrate was washed with 1 M NaOH (2 × 50 ml) and saturated brine solution (50 ml). The organic phrase was dried over Na_2SO_4 and the solvent was removed under reduced pressure. Then 50 ml hexane was added to the resulting residue and stirred overnight at room temperature. The solution was filtered through a Celite pad. Removal of the solvent under reduced pressure gave the desired ligand as a yellow oil. Yield: 201 mg (47%). ESI-MS: *m*/*z* 280 $[M + H]^+$; 302 $[M + Na]^+$. ^{1}H-NMR (500 MHz, $CDCl_3$) δ (ppm): 5.74 (s, 1H), 4.01 (t, 2H), 2.91 (t, 2H), 2.76–2.74 (m, 4H), 2.65 (s, 4H), 2.64–2.62 (m, 4H), 2.34 (s, 6H), 2.22 (s, 3H), 2.19 (s, 3H); ^{13}C-NMR (125 MHz, $CDCl_3$) δ (ppm): 147.2, 138.6, 104.8, 58.2, 57.5, 56.9, 56.2, 47.0, 46.7, 13.4, 11.7.

Synthesis of ^{Me2,Me}ImTACN [1-((1-methyl-1*H*-imidazol-1-yl)methyl)-4,7-dimethyl-1,4,7-triazacyclononane]. The 1,4-dimethyl-1,4,7-triazacyclononane·3HBr salt was converted to the corresponding free base using NaOH followed by extraction with CH_2Cl_2. A mixture of 1-(2-chloromethyl)-2-methylimidazole hydrochloride (166 mg, 1.0 mmol, 1.0 equiv.), 1,4-dimethyl-1,4,7-triazacyclononane (157.2 mg, 1.0 mmol, 1.0 equiv.) and K_2CO_3 (268 mg, 2.0 mmol, 2.0 equiv.) in extra dry CH_3CN were refluxed for about 20 h under N_2 atmosphere. The resulting yellow solution was then filtered through a Celite pad and the Celite pad was washed with $CHCl_3$. The filtrate was evaporated under reduced pressure and the resulting residue was stirred overnight with hexane (30 ml) and a small amount of CH_2Cl_2

 This journal is © The Royal Society of Chemistry 2023

Open Access Article. Published on 05 January 2023. Downloaded on 11/6/2025 11:33:04 PM.
This article is licensed under a Creative Commons Attribution 3.0 Unported Licence.

(5 ml) at room temperature. The solution was filtered through a Celite pad and removal of the solvent gave the ligand as yellow oil. Yield: 138 mg (55%). ESI-MS: *m/z* 252.1 $[M + H]^+$. ^{1}H-NMR (500 MHz, $CDCl_3$) δ (ppm): 6.87 (s, 1H), 6.8 (s, 1H), 3.71 (s, 3H), 3.66 (s, 2H), 2.75–2.73 (m, 4H), 2.67 (s, 4H), 2.59–2.57 (m, 4H), 2.29 (s, 6H); ^{13}C-NMR (125 MHz, $CDCl_3$) δ (ppm): 146.1, 127.0, 121.3, 57.0, 56.7, 55.7, 55.0, 46.5, 33.0.

Synthesis of $[Fe^{II}(^{Me2,Me2}PyzTACN)(CF_3SO_3)_2]$ (1^{Pz}). A solution of ^{Me2,Me2}**PyzTACN** (190 mg, 0.68 mmol, 1.0 equiv.) in THF (1.0 ml) was added to a solution of $[Fe^{II}(CH_3CN)_2(CF_3SO_3)_2]$ (296 mg, 0.68 mmol, 1.0 equiv.) in THF (2.0 ml) and stirred overnight at room temperature inside a glove box. A white solid was precipitated which was filtered off and washed with THF (2 × 2 ml). After this, it was dissolved in CH_2Cl_2/CH_3CN (3.0 ml per three drops) and filtered through Celite. Removal of the solvent under reduced pressure gave the desired complex as a white solid. Yield: 199 mg (41%). X-ray quality crystals were grown by slow diffusion of ether into a solution of the metal complex in CH_2Cl_2 with a few drops of CH_3CN. HRMS (*m/z*) 167.5903 $[Fe^{II}(^{Me2,Me2}PyzTACN)]^{2+}$ (calc. 167.5881) (z = 2); 484.1303 $[Fe^{II}(^{Me2,Me2}PyzTACN)(CF_3SO_3)]^+$ (calc. 484.1287) (z = 1); Elemental analysis $C_{17}H_{29}F_6N_5O_6S_2Fe$ (MW = 633.406 g mol^{-1}) Calc. (%) C 32.24, H 4.61, N 11.06; Found (%) C 33.09, H 4.92, N 10.83; ^{1}H-NMR (400 MHz, CD_3CN) 130.4, 98.4, 66.5, 52.5, 34.6, 34.0, 13.5, −3.41; UV/Vis λ (nm) 194 (ε = 8327 M^{-1} cm^{-1}), 220 (ε = 6922 M^{-1} cm^{-1}); FTIR (KBr) ν (cm^{-1}) 2963–2863, 1672, 1558, 1501, 1474, 1430, 1371, 1355, 1324, 1293, 1233, 1163, 1133, 1090, 1070, 1061, 1030, 910, 804, 788, 776, 759, 751, 638, 576, 516.

Synthesis of $[Fe^{II}(^{Me2,Me}ImTACN)(CF_3SO_3)_2]$ (1^{Im}). A solution of ^{Me2,Me}**ImTACN** (125.6 mg, 0.5 mmol, 1.0 equiv.) in THF (1.0 ml) was added to a solution of $[Fe^{II}(CH_3CN)_2(CF_3SO_3)_2]$ (217.6 mg, 0.5 mmol, 1.0 equiv.) in THF (1.5 ml) and stirred overnight at room temperature inside a glove box. The colour of the solution changed to pale yellow. The reaction solution was evaporated under vacuum and the residue was dissolved in CH_2Cl_2/CH_3CN (4 : 1 mixture) and filtered through Celite. Diffusion of ether into the resultant solution resulted in precipitation of the complex as a light yellowish white solid. Yield: 137 mg (45%). HRMS (*m/z*) 153.5751 $[Fe^{II}(^{Me2,Me}ImTACN)]^{2+}$ (calc. 153.5724) (z = 2); 456.0970 $[Fe^{II}(^{Me2,Me}ImTACN)(CF_3SO_3)]^+$ (calc. 456.0974) (z = 1); Elemental analysis $C_{15}H_{25}F_6N_5O_6S_2Fe$ (MW = 605.353 g mol^{-1}) Calc. (%) C 29.76, H 4.16, N 11.57; Found (%) C 30.55, H 4.28, N 11.08; ^{1}H-NMR (500 MHz, CD_3CN) 99.43, 82.93, 69.52, 64.56, 55.36, 50.00, 33.54, 21.24, 6.72, 4.06, 3.65, 3.59, 3.05–3.02, 2.88–2.82, 2.77–2.74, 2.66, 2.59, 2.51–2.48, 2.21, 1.94, 1.81, 1.56, 1.32, 1.24, 1.21, 0.05; UV/Vis λ (nm) 365 (ε = 3100 M^{-1} cm^{-1}), 512 (ε = 60 M^{-1} cm^{-1}); FTIR (KBr) ν (cm^{-1}) 2921, 1634, 1458, 1259, 1176, 1032, 756, 642, 580, 519.

Crystal structure determination for complex 1^{Pz}

Colourless crystals of 1^{Pz} were grown from slow diffusion of ethyl ether in a CH_2Cl_2 solution of the compound, and used for low temperature (100(2) K) X-ray structure determination. The measurement was carried out on a BRUKER SMART APEX CCD diffractometer using graphite-monochromated Mo Kα radiation (λ = 0.71073 Å) from an X-ray tube. The measurements were made in the range 1.636 to 28.083° for θ. Hemisphere data collection was carried out with ω and φ scans. A total of 16 414 reflections were collected of which 6388 [R(int) = 0.0502] were unique. Programs used: data collection, Smart;[44] data reduction, Saint+;[45] absorption correction, SADABS.[46] Structure solution and refinement was done using SHELXTL.[47]

The structure was solved by direct methods and refined by full-matrix least-squares methods on F^2. The non-hydrogen atoms were refined anisotropically. The H-atoms were placed in geometrically optimized positions and forced to ride on the atom to which they are attached. A considerable amount of electron density attributable to a disordered ethyl ether solvent molecule per asymmetric unit was removed with the SQUEEZE option of PLATON.[48] Those solvent molecules are, however, included in the reported chemical formula and derived values (*e.g.* formula weight, F(000), *etc.*).

Reaction conditions for catalysis experiments

In a typical reaction, 360 μL of H_2O_2 (25 μmol), taken from a 70 mM H_2O_2 stock solution in CH_3CN together with 45 μL of water (2500 μmol), was delivered by syringe pump over 30 min at room temperature under air to a vigorously stirred CH_3CN solution (2.14 ml) containing the Fe-catalyst (2.5 μmol) and the alkane substrate (2500 μmol). The final concentrations were 1 mM for catalyst, 10 mM for the oxidant, 1000 mM for H_2O and 1000 mM for substrate (1 : 10 : 1000 : 1000 for cat : ox : H_2O : sub). For adamantane, due to the low solubility, only 50 μmol of the substrate was used and so the final concentration was 20 mM. At the conclusion of the syringe pump addition, 500 μL of a biphenyl solution of a known concentration (~25 mM) was added to the reaction mixture as an internal standard. The reaction mixture was then passed through a small silica column (to remove the iron complex), followed by elusion with 2 ml ethyl acetate. Finally, the solution was subjected to GC analysis. The organic products were identified and their yields were calculated by using authentic compounds as quantitative standards.

For the measurement of kinetic isotope effects (KIE), a substrate mixture of cyclohexane : cyclohexane-d_{12} in a ratio of 1 : 3 was used to improve the accuracy of the obtained KIE value.

Isotope labeling studies

Catalytic reaction conditions using $H_2{}^{18}O$. In a typical reaction, 290 μL of H_2O_2 (20 μmol), taken from a 70 mM H_2O_2 stock solution in CH_3CN, was delivered by syringe pump over 30 min at room temperature under air to a vigorously stirred CH_3CN solution (1.71 ml) containing the Fe-catalyst (2.0 μmol), substrate (2000 μmol) and $H_2{}^{18}O$ (2000 μmol). The final concentrations were 1 mM for catalyst, 10 mM of the oxidant, 1000 mM for $H_2{}^{18}O$ and 1000 mM for substrate (1 : 10 : 1000 : 1000 for cat : H_2O_2 : $H_2{}^{18}O$: sub). For adamantane, due to the low solubility, only 50 μmol of the substrate was used and so the final concentration was 20 mM.

Open Access Article. Published on 05 January 2023. Downloaded on 11/6/2025 11:33:04 PM.
This article is licensed under a Creative Commons Attribution 3.0 Unported Licence.

Catalytic reaction conditions using $H_2{}^{18}O_2$. In a typical reaction, 34 μL of $H_2{}^{18}O_2$ (20 μmol) taken from a 2% (wt/wt) $H_2{}^{18}O_2$ solution in $H_2{}^{18}O$ was delivered by syringe pump over 30 min at room temperature under air to a vigorously stirred CH_3CN solution (2 ml) containing the Fe-catalyst (2.0 μmol), substrate (2000 μmol) and 45 μL of H_2O. The final concentrations were 1 mM for catalyst, 10 mM for the oxidant, 1000 mM for H_2O and 1000 mM for substrate (1 : 10 : 1000 : 1000 for cat : $H_2O_2{}^{18}$: H_2O : sub).

In the oxidation of adamantane and *cis*-1,2-dimethylcyclohexane, the solution (after syringe pump addition) was passed through a small silica column to remove the Fe-catalyst, followed by elution with 2 ml ethyl acetate. For other substrates, the reaction solution was treated with 1 ml acetic anhydride and 0.1 ml of 1-methylimidazole to esterify the alcohol products for GC-MS analyses (tertiary alcohols are not esterified under these conditions). Samples were concentrated by removing part of the solvent under vacuum and subjected to GC-MS analyses.

Computational details and modeling

All DFT calculations were carried out with the Gaussian 09 package of programs[49] using the B3LYP hybrid functional. This functional is comprised of Becke's three-parameter hybrid exchange functional (B3)[50] and the correlation functional of Lee, Yang, and Parr (LYP).[51] The iron atom was described with the Stuttgart–Dresden effective core potential and SDD basis set,[52,53] and the 6-31G(d′) basis set[54,55] was employed for all remaining atoms.

All reported geometries were fully optimized, and analytical second derivatives were evaluated at each stationary point to determine whether the geometry was an energy minimum (no negative eigenvalues) or a transition structure (one negative eigenvalue). Unscaled vibrational frequencies were used to make zero-point and thermal corrections to the electronic energies. The resulting potential energies and enthalpies are reported in kcal mol^{-1} relative to the specified standard. Standard state corrections were applied to all species to convert concentrations from 1 atm to 1 M according to the treatise of Cramer.[56] The geometry-optimized structures have been drawn with the JIMP2 molecular visualization and manipulation program.[57,58]

Calculation of buried volume

Calculations of buried volume were carried out using the online version of the SambVca 2.1 program (**https://www.molnac.unisa.it/OMtools/sambvca2.1/index.html**).[59] Atomic radii were chosen as Bondi radii scaled by a factor of 1.17; the sphere radius was 3.5 Å around origo; the mesh spacing for numerical integration was 0.10; all hydrogen atoms of the ligand were included in the calculation. For each molecule, the position of the iron ion was chosen as origo, the iron-oxygen ($\mathbf{O_B}$) axis was chosen as the positive *z*-axis direction, and the iron-N(heterocycle) axis was chosen as the *X*-axis.

Conflicts of interest

There are no conflicts of interest.

Acknowledgements

This research has been carried out within the frameworks of the International Research Training Group Metal sites in biomolecules: structures, regulation and mechanisms and COST Action CM1003. MM thanks the European Commission for an Erasmus Mundus fellowship. YL thanks the Chinese Scholarship Council for a predoctoral fellowship. MGR acknowledges financial support from the Robert A. Welch Foundation (grant B-1093-MGR). Computational resources through the High-Performance Computing Services and CASCaM at the University of North Texas are acknowledged. This paper is dedicated to the memory of Professor Gábor Speier, a pioneer in bio-inspired coordination chemistry and biomimetic oxidation catalysis.

References

1 P. Gandeepan, T. Muller, D. Zell, G. Cera, S. Warratz and L. Ackermann, *Chem. Rev.*, 2019, **119**, 2192–2452.
2 Z. Shi, C. Zhang, C. Tang and N. Jiao, *Chem. Soc. Rev.*, 2012, **41**, 3381–3430.
3 A. Furstner, *ACS Cent. Sci.*, 2016, **2**, 778–789.
4 L. Que Jr. and W. B. Tolman, *Nature*, 2008, **455**, 333–340.
5 C. Perry, E. L. C. de los Santos, L. M. Alkhalaf and G. L. Challis, *Nat. Prod. Rep.*, 2018, **35**, 622–632.
6 S. M. Barry and G. L. Challis, *ACS Catal.*, 2013, **3**, 2362–2370.
7 E. G. Kovaleva and J. D. Lipscomb, *Nat. Chem. Biol.*, 2008, **4**, 186–193.
8 M. Costas, M. P. Mehn, M. P. Jensen and L. Que Jr., *Chem. Rev.*, 2004, **104**, 939–986.
9 S. Chakrabarty, R. N. Austin, D. Deng, J. T. Groves and J. D. Lipscomb, *J. Am. Chem. Soc.*, 2007, **129**, 3514–3515.
10 P. R. Ortiz de Montellano, *Chem. Rev.*, 2010, **110**, 932–948.
11 G. Olivo, O. Cusso, M. Borrell and M. Costas, *J. Biol. Inorg. Chem.*, 2017, **22**, 425–452.
12 O. Lyakin, K. P. Bryliakov and E. P. Talsi, *Coord. Chem. Rev.*, 2019, **384**, 126–139.
13 S. Kal, S. Xu and L. Que Jr., *Angew. Chem., Int. Ed.*, 2020, **59**, 7332–7349.
14 J. Chen, Z. Jiang, S. Fukuzumi, W. Nam and W. Bing, *Coord. Chem. Rev.*, 2020, **421**, 213443.
15 A. A. Shteinman and M. Mitra, *Inorg. Chim. Acta*, 2021, **523**, 120388.
16 A. Company, L. Gomez, M. Guell, X. Ribas, J. M. Luis, L. Que Jr. and M. Costas, *J. Am. Chem. Soc.*, 2007, **129**, 15766–15767.
17 A. Company, L. Gomez, X. Fontrodona, X. Ribas and M. Costas, *Chem. – Eur. J.*, 2008, **14**, 5727–5731.

 This journal is © The Royal Society of Chemistry 2023

Open Access Article. Published on 05 January 2023. Downloaded on 11/6/2025 11:33:04 PM.
This article is licensed under a Creative Commons Attribution 3.0 Unported Licence.

18 I. Prat, A. Company, V. Postils, X. Rivas, L. Que Jr., J. M. Luis and M. Costas, *Chem. – Eur. J.*, 2013, **19**, 6724–6738.
19 I. Prat, J. S. Mathienson, M. Guell, X. Ribas, J. M. Luis, M. Cronin and M. Costas, *Nat. Chem.*, 2011, **3**, 788–793.
20 I. Prat, A. Company, T. Corona, T. Parella, X. Ribas and M. Costas, *Inorg. Chem.*, 2013, **52**, 9229–9244.
21 M. Mitra, J. Lloret-Fillol, M. Haukka, M. Costas and E. Nordlander, *Chem. Commun.*, 2014, **50**, 1408–1410.
22 A. Diebold and K. S. Hagen, *Inorg. Chem.*, 1998, **37**, 215–223.
23 D. W. Blakesley, S. C. Payne and K. S. Hagen, *Inorg. Chem.*, 2000, **39**, 1979–1989.
24 K. Chen and L. Que Jr., *J. Am. Chem. Soc.*, 2001, **123**, 6327–6337.
25 G. J. P. Britovsek, J. England and A. P. J. White, *Inorg. Chem.*, 2005, **44**, 8125–8134.
26 A. J. Simaan, S. Dopner, F. Banse, S. Bourcier, G. Bouchoux, A. Boussac, P. Hildebrandt and J. J. Girerd, *Eur. J. Inorg. Chem.*, 2000, 1627–1633.
27 P. Spannring, I. Prat, M. Costas, M. Lutz, P. C. A. Bruijnincx, B. M. Weckhuysen and R. J. M. Klein Gebbink, *Catal. Sci. Technol.*, 2014, **4**, 708–716.
28 J. England, G. J. P. Britovsek, N. Rabadia and A. J. P. White, *Inorg. Chem.*, 2007, **46**, 3752–3767.
29 J. England, C. R. Davies, M. Banaru, A. J. P. White and G. J. P. Britovsek, *Adv. Synth. Catal.*, 2008, **350**, 883–897.
30 J. England, R. Gondhia, L. Bigorra-Lopez, A. R. Petersen, A. J. P. White and G. J. P. Britovsek, *Dalton Trans.*, 2009, 5319–5334.
31 P. Comba, M. Maurer and P. Vadivelu, *Inorg. Chem.*, 2009, **48**, 10389–10396.
32 M. Costas, K. Chen and L. Que Jr., *Coord. Chem. Rev.*, 2000, **200–202**, 517–544.
33 P. Comba and G. Rajaraman, *Inorg. Chem.*, 2008, **47**, 78–93.
34 P. Comba, M. Maurer and P. Vadivelu, *Inorg. Chem.*, 2009, **48**, 10389–10396.
35 K. Chen, M. Costas, J. Kim, A. K. Tipton and L. Que Jr., *J. Am. Chem. Soc.*, 2002, **124**, 3026–3035.
36 K. B. Cho, H. Hirao, S. Shaik and W. Nam, *Chem. Soc. Rev.*, 2016, **45**, 1197–1210.
37 K. B. Cho, X. Wu, Y. M. Lee, Y. H. Kwon, S. Shaik and W. Nam, *J. Am. Chem. Soc.*, 2012, **134**, 20222–20225.
38 V. Postils, A. Company, M. Sola, M. Costas and J. M. Luis, *Inorg. Chem.*, 2015, **54**, 8223–8236.
39 A. Gomez-Suarez, D. J. Nelson and S. P. Nolan, *Chem. Commun.*, 2017, **53**, 2650–2660.
40 G. Esquius, J. Pons, R. Yanez, J. Ros, R. Mathieu, B. Donnadieu and N. Lugan, *Eur. J. Inorg. Chem.*, 2002, 2999–3006.
41 C. Robinson, J. Zhang, D. Garrod, T. Perrior, G. Newton, K. Jenkins, R. Beevers, M. Major and M. Stewart, Pyruvamide Compounds as Inhibitors of Dust Mite Group 1 Peptidase Allergen and their Use, US2012/0322722Al, 2011.
42 D. A. Valyaev, S. Clair, L. Patrone, M. Abel, L. Porte, O. Chuzel and J.-L. Parrain, *Chem. Sci.*, 2013, **4**, 2815–2821.
43 C. Flassbeck and K. Wieghart, *Z. Anorg. Allg. Chem.*, 1992, **608**, 60–68.
44 *Bruker Advanced X-ray Solutions. SMART: Version 5.631*, 1997–2002.
45 *Bruker Advanced X-ray Solutions. SAINT+, Version 6.36A*, 2001.
46 G. M. Sheldrick, *Empirical Absorption Correction Program*, Universität Göttingen, 1996; *Bruker Advanced X-ray Solutions. SADABS Version 2.10*, 2001.
47 G. M. Sheldrick, *Program for Crystal Structure Refinement*, Universität Göttingen, 1997; *Bruker Advanced X-ray Solutions. SHELXTL Version 6.14*, 2000–2003; G. M. Sheldrick, *SHELXL-2013*, 2013.
48 A. L. Spek, *PLATON, A Multipurpose Crystallographic Tool*, Utrecht University, Utrecht, The Netherlands, 2005.
49 M. J. Frisch, *et al.*, *Gaussian 09, Revision E.01*, Gaussian, Inc., Wallingford, CT, USA, 2009.
50 A. D. Becke, *J. Chem. Phys.*, 1993, **98**, 5648–5652.
51 C. Lee, W. Yang and R. G. Parr, *Phys. Rev. B: Condens. Matter Mater. Phys.*, 1988, **37**, 785–789.
52 M. Dolg, U. Wedig, H. Stoll and H. Preuss, *J. Chem. Phys.*, 1987, **86**, 866–872.
53 S. P. Walch and C. W. Bauschlicher, *J. Chem. Phys.*, 1983, **78**, 4597–4605.
54 G. A. Petersson, A. Bennett, T. G. Tensfeldt, M. A. Al-Laham, W. A. Shirley and J. Mantzaris, *J. Chem. Phys.*, 1988, **89**, 2193–2218.
55 G. A. Petersson and M. A. Al-Laham, *J. Chem. Phys.*, 1991, **94**, 6081–6090.
56 C. J. Cramer, *Essentials of Computational Chemistry*, Wiley, Chichester, UK, 2nd edn, 2004.
57 M. B. Hall and R. F. Fenske, *Inorg. Chem.*, 1972, **11**, 768–775.
58 J. Manson, C. E. Webster and M. B. Hall, *JIMP2, version 0.091, a free program for the visualization and manipulation of molecules*, Texas A&M University, College Station, TX, 2006, **https://www.chem.tamu.edu/jimp2/index.html**.
59 L. Falivene, Z. Cao, A. Petta, L. Serra, A. Poater, R. Oliva, V. Scarano and L. Cavallo, *Nat. Chem.*, 2019, **11**, 872–879.